24th Symposium on Naval Hydrodynamics
Fukuoka, JAPAN, 8-13 July 2002

Hydrofoil Near-wake Structure and Dynamics at High Reynolds Number

Dwayne A. Bourgoyne, Joshua M. Hamel, Carolyn Q. Judge,
Steve L. Ceccio, David R. Dowling
(Department of Mechanical Engineering, University of Michigan, USA)

J. Michael Cutbirth
(Naval Surface Warfare Center, Carderock Division, USA)

ABSTRACT

Methods to predict the hydrodynamic performance of lifting surfaces at full-scale Reynolds number (chord-based $Re_C \sim 10^8$) have been limited by the scarcity of controlled experimental data for incompressible flow. This paper describes results from the second and third phases of an experimental effort to identify and measure the dominant flow features near the trailing edge of a large hydrofoil at Re_C approaching 10^8. The experiments were conducted at the US Navy's William B. Morgan Large Cavitation Channel employing a two-dimensional hydrofoil (2.1 m chord, 3.0 m span) at flow speeds from 0.25 to 18.3 m/s, yielding Re_C ranging from 0.5 to 61 million. The hydrofoil section is a modified NACA 16, designed to approximate the cross section of a generic naval propeller blade, with the capacity for testing different trailing shapes. Bourgoyne *et al*. (2001A) reported observations of the mean flow, turbulent flow statistics, and mean surface pressure for the hydrofoil's baseline trailing edge. Presented here are observations of the hydrofoil's unsteady near-wake and the unsteady surface pressures on the trailing edge for both a baseline and a modified trailing edge configuration. The results include PIV-acquired vector fields, surface dynamic pressure spectra, and LDV-acquired velocity spectra from the separating boundary layer and near wake. Trailing edge geometry and Reynolds number dependencies (Re-dependencies) of the vortex shedding are demonstrated in instantaneous vector fields and in velocity and pressure spectra. Shedding intensity is found to correlate with the mean suction side shear layer velocity gradient and possibly with suction/pressure side shear layer symmetry. Variation in the mean suction side shear layer gradient is shown to be the result of the Re-dependence of the laminar to turbulent transition and growth of the suction side boundary layer.

INTRODUCTION

Lifting surfaces are used both for propulsion and control of ships and must meet performance criteria such as lift, drag, vibration, and hydroacoustic noise. Design tools suitable to predict such criteria must handle complex flow phenomena and manage the wide range of scales inherent in marine applications. To date, the development of such tools has been limited by the scarcity of controlled experimental data for incompressible flows with chord-based Reynolds numbers, ($\mathrm{Re}_C \equiv UC/\nu \approx 10^8, C \equiv chord$) exceeding several million. A research effort was therefore initiated to examine the flow over a large two-dimensional hydrofoil (the HIFOIL project). A principal goal of this effort is to provide a detailed set of measurements that can be used to formulate and validate numerical models for use at high Re.

The two-dimensional HIFOIL model has a NACA-16 derived suction side surface and a beveled trailing edge, features representative of a naval propeller blade of moderate thickness and chamber. This cross section is both application-relevant and potentially rich in Re-dependent flow features. In particular, this shape allows examination of wake-vortex formation, or *vortex shedding*, and its Re-dependence. Relatively small modifications to the trailing edge geometry are known to lead through the enhancement or suppression of wake vortices to substantial changes in hydrofoil performance (Blake, 1986). The application of a bevel (or *knuckle*) to the trailing edge can modify the shedding of the wake vortices. This, in turn, can substantially change the magnitude and spectrum of the acoustic energy

generated by the wake. A high sensitivity of shedding to trailing edge geometry suggests a similar sensitivity to the properties of the trailing edge boundary layers and initial separated shear layers. Aspects of boundary layer growth, separation, and shear layer development are potentially Re-dependent. Thus, significant changes in Reynolds number may lead to significant changes in the near wake shedding.

Besides serving as a test case for numerical models, trailing edge vortex shedding is a phenomenon requiring greater fundamental understanding. In addition to impacting lift and drag, near wake shedding is one of the main hydroacoustic noise sources from a fully submerged non-cavitating lifting surface. Moreover, when there is feedback between the vortex shedding drive (associated with the Kelvin-Helmholtz instability) and a structural vibrational mode, excessive noise and potentially damaging vibration (singing) may occur. To date, the details of this hydrodynamic forcing and subsequent structural response are largely un-documented at the Reynolds number of many marine propulsion applications. Prior work on the shedding problem has focused on non-lifting bodies fitted with propulsor-like trailing edges and limited to Re_C of several million (Blake, 1986). By incorporating a realistic suction side surface and hence a major portion of the lift, the HIFOIL shape serves as the next step toward a fully representative propulsor model. It further extends the Re_C of the available data to near full-scale. Researchers have already computed both the flow field and the noise generated by minimally lifting surfaces (Wang *et al*. 1996, Arabshahi *et al*. 1999) and plan to extend this work to the HIFOIL shapes.

EXPERIMENTAL SET-UP

The hydrofoil was designed for use in the U.S. Navy's William B. Morgan Large Cavitation Channel (LCC) in Memphis, Tennessee. The largest facility of its kind in the world, the LCC is a low turbulence re-circulating water tunnel with a 3.05 m × 3.05 m × 13 m test section capable of steady flows from 0.25 to 18.3 m/s. The hydrofoil (Fig. 1a) has a chord of 2.13 m, fully spans the test section, and based on its max thickness (0.171 m) presents a flow area blockage factor of 6%. Fig. 1a also depicts the coordinate system used in presenting the data, with the idealized sharp tip of the trailing edge defined as the coordinate (x/C, y/C) = (1, 0). Facility limits for flow speed (18.3 m/s) and water temperature (104° F), yield for the HIFOIL model a Re_C as high as 61 million. A bolt-on trailing edge modifier was used to vary bevel geometry and in turn vary the characteristics of the vortex shedding produced. The two bevel designs tested are shown in Fig.1b: the more streamlined *baseline* trailing edge (bevel radius, R_B=76.2 mm and apex angle, β=44°), and a more bluff *modified* trailing edge (R_B=38.1 mm, β=56°). Both geometries generate suction side boundary layer flow separation in the last 97% of chord. Both shapes are known through Navy experience to generate quasi-periodic vortex shedding without causing excessive hydrofoil vibration.

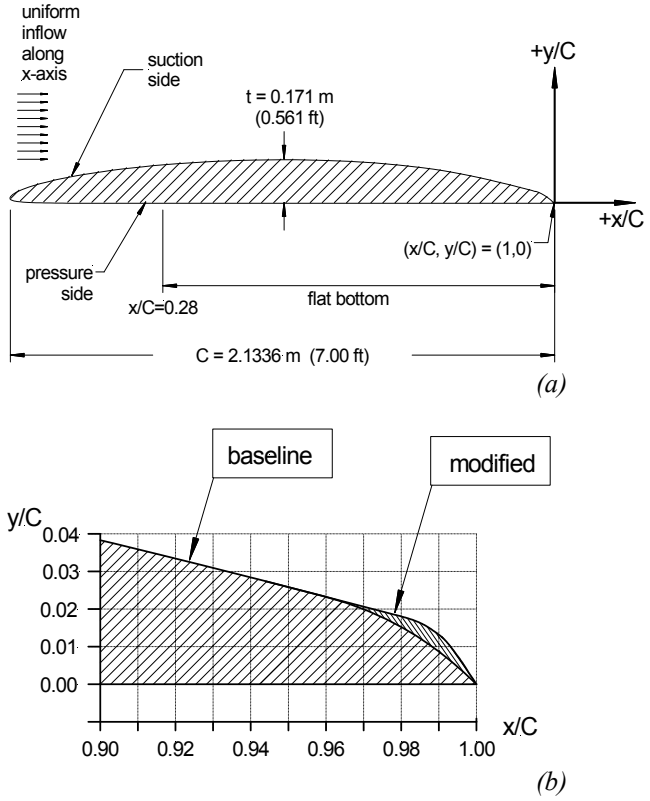


Figure 1. (a)Hydrofoil cross sectional geometry with the coordinate system shown and the coordinate (x/C, y/C) = (1,0) at the trailing edge; (b)Detail of the trailing edge showing the original (baseline) configuration and the modified configuration.

The hydrofoil was machined from a solid Ni-Al Bronze casting and polished to a RMS surface roughness of 0.25 μm or less. Based on estimates from a flat plate boundary layer flow, this represents a k+ < 1 at the highest Reynolds number tested. Thus the hydrofoil may be considered hydrodynamically smooth (White, 1991). For the data presented here, the hydrofoil boundary layer is not artificially tripped, but was allowed to transition to turbulence naturally. Due to the curved suction side surface, the

hydrofoil generates considerable lift: approximately 588 kN at a flow speed of 18.3 m/s and 0° angle of attack. Further detail on the experimental facility and model is provided in previous work (Bourgoyne *et al.*, 2001A, 2001 B).

The test section flow velocity was set through computer control of the rotational speed of the LCC impeller and monitored with a stationary single-component Laser-Doppler Velocimetry (LDV) probe positioned more than two chord lengths upstream of the hydrofoil's leading edge. This LDV probe provided the upstream reference velocity, U_{ref}, used in the data reduction. To support Particle Imaging Velocimetry (PIV), the channel's 5000 m^3 of water was seeded with approximately 20 kg of silver-coated glass spheres of 16 µm mean diameter (Potters Industries, SH400S33). Due to test constraints, both LDV and PIV were taken under identical seeding conditions, though smaller seed is preferable for LDV. Tunnel pressure was held constant and sufficiently high to suppress cavitation. Tunnel temperature was monitored, and water temperature increased as much as 1.3°C/hr during tests at 18.3 m/s. The main impact of temperature variation was to vary water viscosity and hence the Re_C for a given flow speed. Water temperatures for the data presented here ranged from 27 to 33 °C, producing the Re_C ranges shown in Table.1.

U_{ref} [m/s]	0.5	0.75	1.0	1.5	2.25	3.0	6.0	12.0	18.3
Re_C x 10^6	1	2	3	4	6	8	15-17	30-34	46-52

Table 1. Re_C vs. U_{ref} over test temperature range of 27 to 33 °C.

Measurements of the flow on and near the hydrofoil were made with an external two-component LDV (main measuring plane at 1/4 span), static pressure taps, dynamic pressure transducers, and a two-component PIV system (measuring plane at 1/3 span). Accelerometers were mounted within the hydrofoil to monitor vibration. In addition, a separate investigating team measured the streamwise velocity statistics of the suction side boundary layer at x/C = 0.43 using a miniaturized 1-component LDV probe housed within the hydrofoil body (Fourguette, *et al.*, 2001).

The external 2-component LDV system uses Dantec FO probes with 111-mm beam spacing and 1600-mm (in air) focal length. This provides an in-water probe volume of approximately 170 µm in diameter and 6 mm in length. Further details on the external LDV, including estimation of uncertainty and time-averaged statistics from velocity surveys, may be found in prior work. (Bourgoyne, *et al,.* 2001A). The 2-component LDV was also used to gather velocity spectra at selected locations in the wake (Fig. 2, black square symbols). Dantec-provided software (BSA Flow) was used to estimate the power spectrum from the uncorrelated raw velocity data-samples using sample/hold re-sampling and Fast Fourier Transform (FFT) with Hanning windowing. Effective low-pass filtering occurred as a consequence of re-sampling data produced from random particle arrival times. No high-pass filtering was employed, but the maximum re-sampling frequency was maintained at 2-3 times the mean data rate as a compromise between frequency resolution and high-frequency aliasing. Data acquisition and processing parameters defining the uncertainty of these results are presented in App. A.

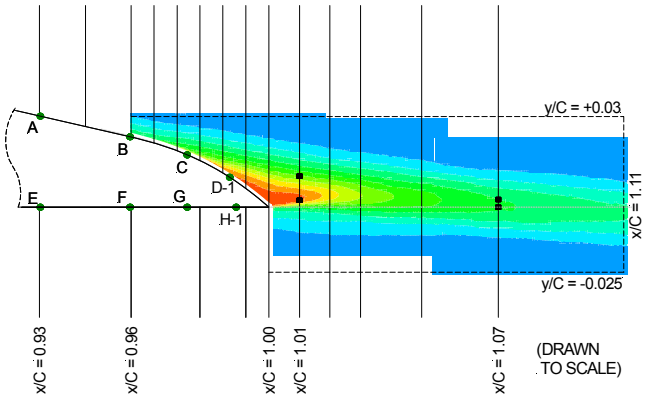


Figure 2. Trailing edge measurement locations. The region of PIV measurement (flow contours), the LDV time-averaged measurement stations (vertical black lines), and the LDV spectral measurement points (black squares) are shown. Unsteady surface pressures are measured at the model surface locations labeled with letters A through H.

The static pressure measurements were made using 30 measuring taps on the hydrofoil and a Rosemont differential pressure transducer routed to individual taps with a Scanivalve rotary sampling valve. Dynamic surface pressure measurements were made with an array of fifteen flush mounted pressure transducers (PCB 138M101) located at the PIV measuring plane and in the vicinity of the hydrofoil trailing edge. These sensors were arrayed in an "L" shape with lines of transducers set parallel (shown in Fig. 2) and perpendicular to the flow direction. Results presented in this paper are from the pressure side transducer 'H-1', nearest the trailing edge. The dynamic pressure signals were analogue band-pass filtered from 2 Hz to 5 kHz and sampled at 10 kHz.

An array of eight accelerometers (Wilcoxon 754-1) was mounted within the hydrofoil to monitor vibration. Accelerometer frequency response was 2 Hz to15 kHz at +/-3dB, were sampled at 10 kHz, and were filtered by a signal conditioner (PR701A) with a frequency response of 0.5 Hz to 1 kHz at -3dB. Results presented in this paper are from accelerometer 'A2' located with the dynamic pressure sensors.

Instantaneous flow field measurements in the vicinity of the hydrofoil trailing edge were made using a LaVision Flowmaster-3S PIV system running DaVis v5.4.4 software and utilizing two flash-lamp pumped YAG lasers (800 mJ per pulse at 532 nm). A laser sheet masked to approximately 3.2 mm thickness was routed downward through the top of the LCC test section to illuminate the suction-side trailing edge and near wake. The pressure side of the hydrofoil was not illuminated. Two 1280 by 1024 pixel cameras were operated in tandem to capture the composite field of view depicted in Fig. 2. Images were acquired at a rate of approximately 1 Hz. For the vector fields presented in this paper, raw images from a single camera were processed via cross-correlation of 32 by 32 pixel interrogation areas with 50% overlap into two-dimensional velocity fields with 1.7-mm grid spacing. Thus each vector is the result of particle pair averaging over a cube of flow measuring approximately 3.4 mm on a side. Further information on the experimental instrumentation is provided in prior work (Bourgoyne *et al*., 2001A, 2001B).

RESULTS- PRESSURE COEFFICIENTS

Flow, pressure, and vibration measurements were made at a variety of test conditions. Presented here are results for test speeds from 0.5 to 18.3 m/s, 0° angle of attack, un-tripped boundary layers, and both the baseline and modified trailing edge geometries. In order to depict the dependence of the vortex shedding on trailing edge geometry and Re_C, emphasis is given to the flow speeds of 0.5, 1.5, and 18.3 m/s.

The pressure coefficient, C_p, on the surface of the hydrofoil was acquired at speeds from 1.5 to 18.3 m/s for both the baseline and modified trailing edges. Acquiring data at a lower speed was not feasible with the pressure sensors used. A representative C_p curve for the modified trailing edge (data averaged over all the measured speeds) is shown in Fig. 3. Also shown is the estimated location of boundary layer laminar to turbulent transition for each flow speed. For all speeds, transition was computed from the mean C_p data of Fig. 3 using Thwaites' method and the 1-step method of Wazzan, *et al.* (White, 1991). Application of the 1-step Wazzan method is consistent with the low freestream turbulence of the LCC and the smooth surface finish of the hydrofoil. The transition results were validated against measurements where data was available. Specifically suction side boundary layer streamwise velocities at x/C=0.43 were measured with the onboard LDV for the baseline trailing edge at flow speeds of 3.0, 6.0, 12.0, and 18. 3 m/s (Fourguette, *et al*., 2001). These boundary layer measurements indicate a fully laminar condition at 3.0 m/s, a transitional or turbulent condition at 6.0 m/s, and a fully turbulent condition at the higher speeds.

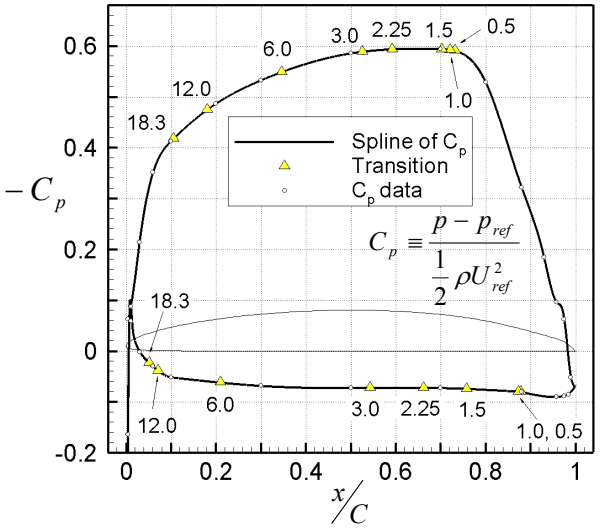


Figure 3. Static pressures coefficients measured on the modified hydrofoil averaged over flow speeds of 1.5 to 18.3 m/s. This data was splined and used to compute the location of natural transition on the hydrofoil.

A significant feature of the C_p curve is immediately apparent: the location of suction side transition at speeds of 1.5 m/s and below is roughly fixed at the C_p "cliff" near x/C~0.75. This has interesting implications concerning the Re_C-dependence of the suction side boundary layer thickness near the trailing edge. Fig. 4a shows the PIV-acquired mean boundary layer velocities at x/C=0.94 for several flow speeds. The velocity, u, is the magnitude parallel to the surface at the given x/C and is normalized by $u(y_{max})$, where y_{max} is the measured point furthest from the hydrofoil surface (and provides the best available estimate of the local freestream). These profiles as well as those at other flows speeds were used to calculate the normalized suction side boundary layer momentum thickness, θ/C, for the modified trailing edge (Fig. 4b). These values of θ/C indicate that the suction side boundary

layer thickness at x/C=0.94 is in some ranges increasing with Re_C and in other ranges decreasing with Re_C. This is due to the dependence of θ/C on the combined effect of the laminar growth rate, the turbulent growth rate, and the location of transition. At speeds above 1.5 m/s, all of these variables are Re-dependent. However, at 1.5 m/s and below, the location of transition becomes approximately fixed on the suction side near x/C ~ 0.75, and only the growth rate variables remain functions of Re. Thus, near 1.5 m/s, there is a trend reversal in the Re_C-dependence of the suction side boundary layer thickness at the trailing edge.

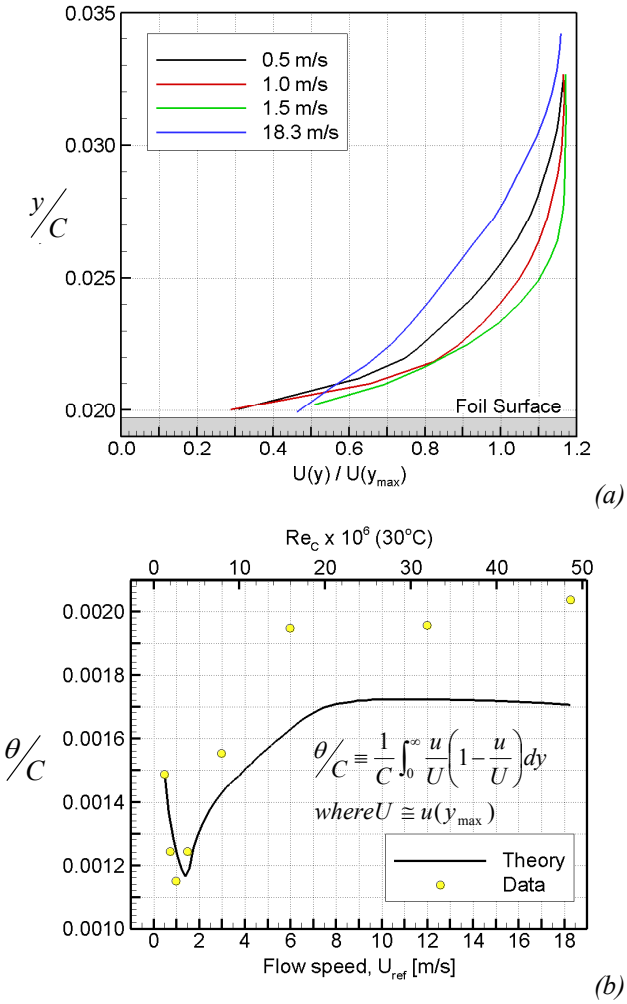


Figure 4. The suction side boundary layer near the trailing edge knuckle (x/C=0.94) with (a) the PIV-acquired mean velocity component parallel to the local surface for four speeds and (b) the measured normalized boundary layer momentum thickness, θ/C vs. flow speed, U_{ref}, for the modified trailing edge geometry. Also shown in (b) are the computed normalized momentum thicknesses.

This proposed role of natural transition in the Re-dependent behavior of θ/C at the trailing edge is substantiated by theory. A prediction of θ/C at the trailing edge, also shown in Fig. 4b, was made using a turbulent boundary layer integral method. Taking the θ/C at transition of Fig. 3a as an initial value, the Karman Integral Relation was solved as described by White (White, 1991), and employing White's relation (eqn. 6-120) for the friction coefficient, C_f. Use of the Thwaites result as an initial condition effectively treats transition as a point, across which θ/C is conserved but all other boundary layer quantities change discontinuously. Despite this simplification, the predicted trend of θ/C is within 10% of the measured values at speeds below 3.0 m/s, and at least follows the measured trend at the higher speeds. The worsening agreement between measurement and theory as the speed increases over 1.5 m/s is attributed to the application of the less accurate turbulent boundary layer relations over an increasing fraction of the chord. Also, there is increasing error in treating transition as a point; the point approximation is nearer to the truth at the speeds where transition occurs at the C_p cliff.

Thus we have established that the momentum thickness of the suction side boundary layer is strongly Re_C-dependent and passes through a minima near 1.5 m/s. The Re_C-dependence of the momentum thickness is explained by the combined effect of the Re_C-dependence of the location of transition and of the laminar and turbulent boundary layer growth rates. The Re_C at which θ/C is minimal is that at which natural transition is approaching the cliff in the Cp curve at x/C~0.75. Following, data will be presented that shows a relationship between the strength of near wake vortex shedding and this Re_C-dependent boundary layer thickness at the trailing edge.

RESULTS- DEPENDENCE OF SHEDDING ON GEOMETRY

Figs. 5 and 6 show PIV-derived contours of the mean streamwise velocity field, normalized by the flow speed U_{ref}=1.5 m/s, for the baseline and modified trailing edges. The mean is taken from 320 images. Flow is from left to right, and the trailing edge is shown on the left side of the frame. Data at the surface suffers from higher uncertainty due to laser glare, so those values are blanked out (white space). No data is available in the shadow below the hydrofoil. Selected vector profiles, also of the normalized streamwise mean, are included to show the downstream evolution of the flow field. The profile at x/C = 1.002 shows the initial shear layer formed by the merging of the suction and pressure

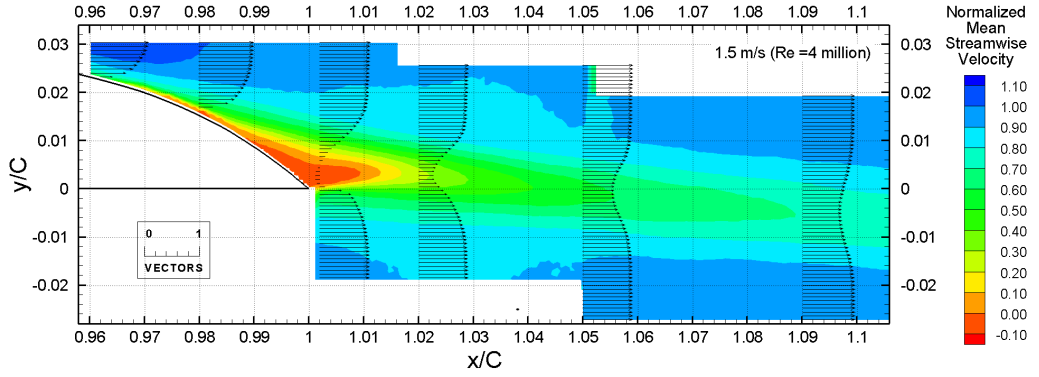


Figure 5. Averaged contours and vector profiles of normalized streamwise velocity, $\overline{u}/U_{ref}$, for the baseline trailing edge at $U_{ref} = 1.5 m/s$. (320 averages)

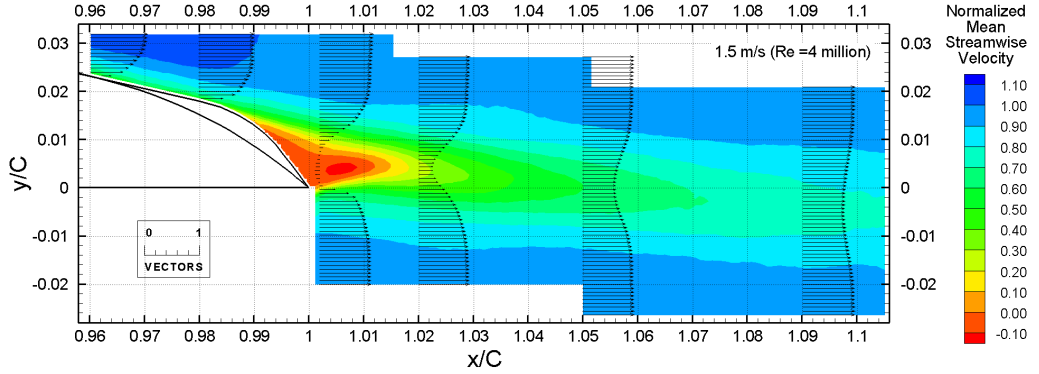


Figure 6. Average contours and vector profiles of normalized streamwise velocity, $\overline{u}/U_{ref}$, for the modified trailing edge at $U_{ref} = 1.5 m/s$. (320 averages)

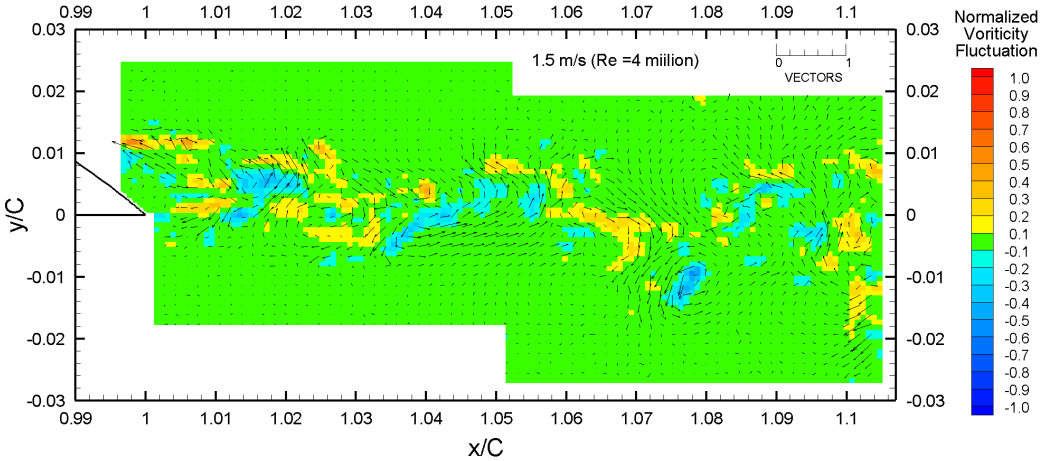


Figure 7. Instantaneous contour of normalized vorticity fluctuation, $(\omega - \overline{\omega})\delta^* / U_{ref}$, and vector field of normalized instantaneous velocity fluctuations, $\left[(u - \overline{u}), (v - \overline{v})\right] / U_{ref}$, for the baseline trailing edge at $U_{ref} = 1.5 m/s$.

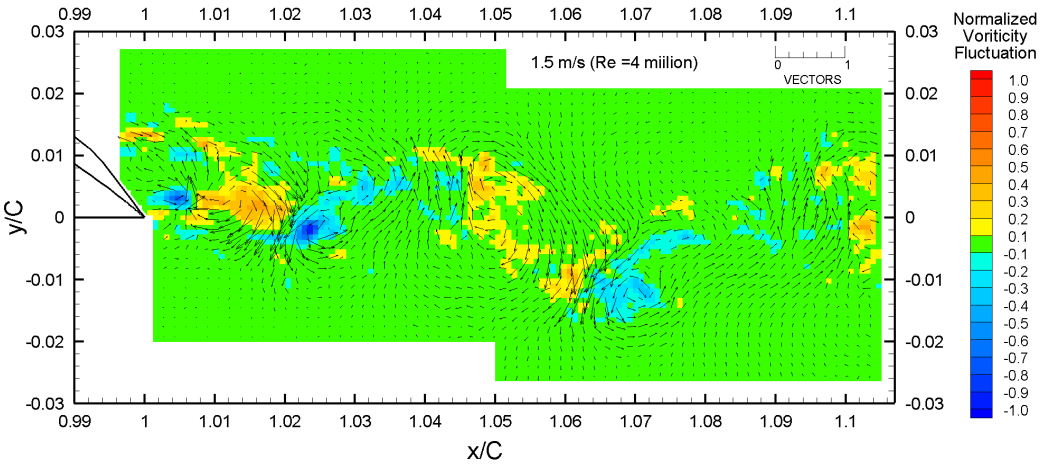
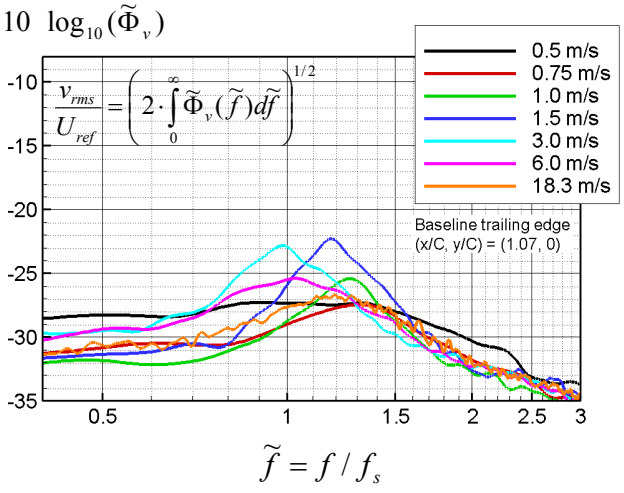


Figure 8. Instantaneous contour of normalized vorticity fluctuation, $(\omega-\overline{\omega})\delta^*/U_{ref}$, and vector field of normalized instantaneous velocity fluctuations, $[(u-\overline{u}),(v-\overline{v})]/U_{ref}$, for the modified trailing edge at $U_{ref}=1.5\,m/s$.

side boundary layers. The differences in this profile between trailing edge geometries should be noted, and will be central to the discussion of the shedding behavior.

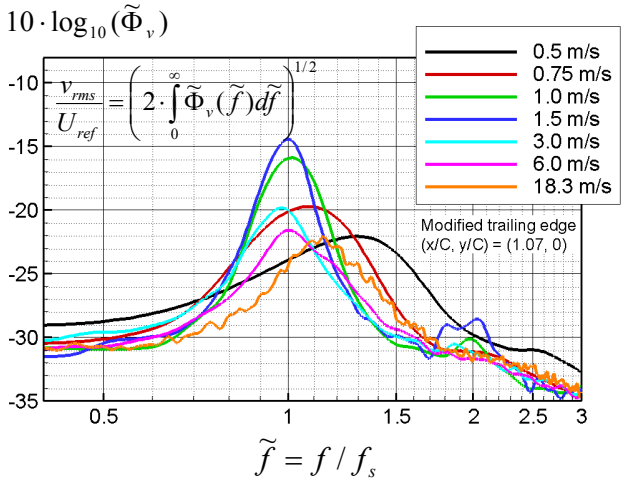
In Figs. 7 and 8, a representative instantaneous velocity field is shown for the same flow condition and geometries. Here, contours are the difference of mean and instantaneous vorticity, normalized using the reference velocity U_{ref} and a nominal pressure side boundary layer displacement thickness, $\delta^*/C= 0.002$. (The same nominal value for δ^*/C is used in all vorticity figures in this paper, allowing direct comparison of vorticity magnitudes at various flow conditions.) The vorticity is calculated using Stoke's line integral, where vorticity at a given grid-point is derived from its eight immediate neighbors. Vectors show the difference of mean and instantaneous velocity. Shedding structures are clearly evident in Fig 8 for the modified trailing edge at 1.5 m/s. This condition and geometry was the strongest shedding condition tested as determined by surface pressure spectra, and was of equivalent strength to 1.0 m/s modified trailing edge condition as determined by velocity spectra. By comparison the vortical structures are largely absent for the baseline trailing edge in Fig 7. In images where such structures do appear, they tend toward higher x/C and did not form the organized "vortex street" of Fig. 8. The appearance at higher x/C of the first organized vortices is consistent with an inverse relationship between shedding strength and vortex formation distance. While 1.5 m/s is the most illustrative case, a similar trend is observed at all test speeds: the appearance of coherent shedding structures increases in going from the baseline to the modified trailing edge.

The vortex structures apparent in Figs. 7 and 8 should also be detectable in the spectral characteristics of the near wake. Figs 9 and 10 show LDV-acquired power spectra of the vertical velocities, estimated from between four and six individual Fast Fourier Transforms (FFT's).



U_{ref} [m/s]	v_{rms}/U_{ref} [%]
0.5	11 +/- 2
0.75	9 +/- 2
1.0	9 +/- 2
1.5	11 +/- 2
3.0	11 +/- 2
6.0	10 +/- 1
18.3	10 +/- 1

Figure 9. Normalized power spectrum of vertical velocity component, $\widetilde{\Phi}_v$, at varying flow speed, U_{ref}, for baseline trailing edge.



U_{ref} [m/s]	v_{rms}/U_{ref} [%]
0.5	13 +/- 2
0.75	13 +/- 2
1.0	14 +/- 2
1.5	15 +/- 2
3.0	12 +/- 1
6.0	11 +/- 2
18.3	11 +/- 1

Figure 10. Normalized power spectrum of vertical velocity component, $\widetilde{\Phi}_v$, at varying flow speed, U_{ref}, for modified trailing edge.

The data was taken for both trailing edge geometries at x/C coordinates of 1.01 and 1.07, and at y/C coordinates chosen by searching (within test time constraints) for the location of maximum shedding at that x/C. Data from (x/C, y/C) = (1.07, 0) is presented here as a point of reasonably good comparison for all speeds and both trailing edges. Both the power density axis and the frequency axis are normalized by a freestream velocity and a wake thickness y_f, after the fashion of Blake (1986) and defined below:

$$\widetilde{\Phi}_v(\widetilde{f}) \equiv \frac{\Phi_v \cdot f_s}{(U_{ref})^2} \tag{1}$$

$$\widetilde{f} \equiv \frac{f}{f_s} \tag{2}$$

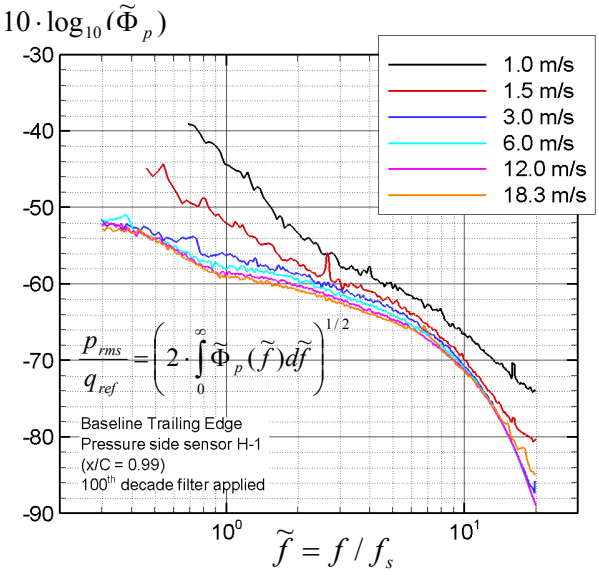
$$f_s \equiv \frac{U_{ref}}{2\pi \cdot y_f} \quad \text{[Hz]} \tag{3}$$

Here, y_f is taken to be a constant value of $y_f/C=0.01$. This is approximately equal to the vertical distance between the peaks in the Reynolds stresses measured in the near wake, as described in Bourgoyne, *et al.* (2001B). Under this normalization shedding appears near a normalized frequency of unity. Further definition of the velocity power density, Φ_v, its uncertainty, and the data acquisition parameters of the individual FFT's are provided in App. A. The relationship of the integral of the power spectrum to the variance is given on the figure on which it is plotted. The normalized v_{rms} values shown are computed directly from this integral and compare favorably with LDV time-averaged statistics taken at the same location during earlier testing (Bourgoyne, *et al.*, 2001A). The uncertainties given with the normalized v_{rms} values provide an indication of the uncertainty of the overall spectra. These values are the RMS of the v_{rms} values computed from the individual FFT's averaged to make the plotted spectrum. Note the relative magnitudes of the 1.5 m/s shedding peaks for the baseline and modified trailing edges. Also note that at all speeds, the shedding is stronger on the modified trailing edge.

The shedding trends in the velocity spectra are in agreement with an independent measurement of the unsteady pressure on the trailing edge surface. The power spectra shown in Figs. 11 and 12 were derived from the flush mounted dynamic pressure sensor H-1, located on the pressure side surface at x/C = 0.99 (see Fig. 2). These spectra are normalized after Blake in a fashion similar to that used for the velocity spectra:

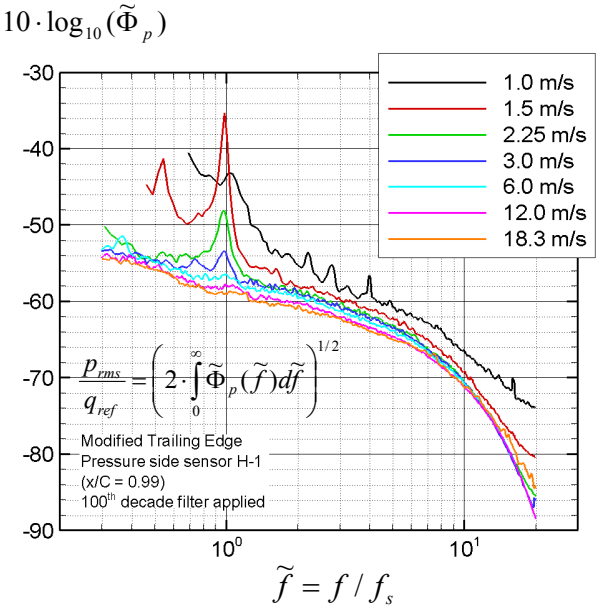
$$\widetilde{\Phi}_p(\widetilde{f}) \equiv \frac{\Phi_p \cdot f_s}{(q_{ref})^2} \tag{4}$$

$$q_{ref} \equiv \frac{1}{2}\rho U_{ref}^2 \quad \text{[Pa]} \tag{5}$$



U_{ref} [m/s]	p_{rms}/q_{inf} [%]
1.0	2.5
1.5	1.0
3.0	0.6
6.0	0.5
12.0	0.4
18.3	0.4

Figure 11. Normalized power spectra of surface pressure, $\tilde{\Phi}_p$, at varying flow speed, U_{ref}, for the pressure side sensor H-1 at x/C=0.99 on the baseline trailing edge.



U_{ref} [m/s]	p_{rms}/q_{inf} [%]
1.0	2.4
1.5	1.1
2.25	0.6
3.0	0.5
6.0	0.4
12.0	0.4
18.3	0.4

Figure 12. Normalized power spectra of surface pressure, $\tilde{\Phi}_p$, at varying flow speed, U_{ref}, for the pressure side sensor H-1 at x/C=0.99 on the modified trailing edge.

Again, the relationship of the power spectrum to the variance is given on the plot. These spectra are estimated from approximately (3)10^6 data points, partitioned with 50% overlap to provide 376 FFT's each of 16,384 points, with an estimated spectral bin uncertainty of approximately 12% (Vetterling, *et. al.*, 1992). A linear least-squares fit has been subtracted from each partition to remove any trend and zero the mean. Neither acceleration contamination nor other noise has been subtracted, and a 1/100th decade filter has been applied to clarify the plots (with negligible effect on peak magnitudes). The upward translation of the curves as velocities fall below 3.0 m/s reflects the increasing fraction of the pressure signal that results from noise and therefore does not scale with velocity.

The shedding peaks seen in the velocity spectra on the modified trailing edge at speeds over 3.0 m/s are not distinctly visible in the pressure spectra of Fig. 12. However, this may be attributed to shedding of insufficient power to be detected above the separated shear layer turbulence. As speed is reduced to below 3.0 m/s, peaks rise above this background level to reveal a maximum detected shedding condition at 1.5 m/s. The curve at 1.0 m/s is compromised by poor signal-to-noise including a strong noise peak near a normalized frequency of 0.5, and fails to confirm or discount the 1.0 m/s peak seen in the velocity spectra. Data from speeds below 1.0 m/s is dominated by noise and is not presented. By comparison, the pressure spectra for the baseline trailing edge (Fig. 11) entirely lack peaks (except those attributed to noise or vibration), indicating no shedding detectable above the turbulence of the separated shear layers. Further discussion of the baseline trailing edge pressure spectra at speeds 3.0 m/s and above, including comparison with historical data, is provided in (Bourgoyne, *et. al.*, 2000B).

The correlation of shedding strength with these trailing edge geometries is consistent with prior

work in the field. A comparison of shedding strength from minimally-lifting bodies with various trailing edge shapes (Table 11-2 in Blake, 1986) suggests that symmetry between the upper and lower shear layers plays an important role. This might be attributed to the ability of the shear layers to cooperate and roll up at a common frequency. Among the more symmetric shapes, those expected to produce sharper mean shear layer velocity gradients are also found to shed more strongly. This trend makes sense from the standpoint of shear layer stability. A correlation of mean shear layer gradient to shedding strength is also found with shedding behind circular cylinders. With this in mind, Fig. 13 re-plots on common axes the normalized mean streamwise velocity profiles at x/C=1.002 from Figs. 5 and 6. (These profiles and those of Fig. 16 are normalized by the upstream flow speed, U_{ref}, and do not collapse to the same normalized velocity at the edges of the boundary layers. This is attributed to the hydrofoil lift and resulting potential flow effects in the test section.) The profile for the modified trailing edge (stronger shedding) has a slightly steeper suction side gradient and has the greater symmetry between suction and pressure side shear layers. This coincidence, however, is not sufficient to demonstrate causality, given that both the stronger shear gradient and the increased shedding may be separate effects of the trailing edge geometry. However, data will be presented next which strengthens the case for a mean shear layer gradient and shedding correlation.

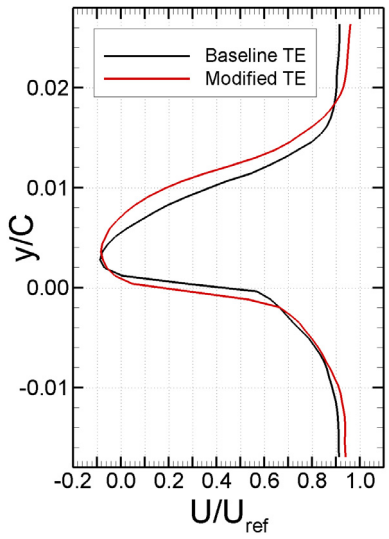


Figure 13. Comparison of normalized mean streamwise velocity profiles, $\overline{u}/U_{ref}$, for the baseline and modified trailing edges at x/C=1.002 and $U_{ref} = 1.5 m/s$.

RESULTS- DEPENDENCE OF SHEDDING ON REYNOLDS NUMBER

In addition to showing dependence of vortex shedding on trailing edge geometry, Figs. 10 and 12 demonstrate a clear dependence in the velocity and pressure spectra on flow speed. Consider the modified trailing edge and its maximum shedding condition of 1.5 m/s, shown in Figs. 6 and 8 as mean and instantaneous flow fields. For comparison, Figs. 14 and 15 show the same plots for the lesser shedding condition of 18.3 m/s on the modified edge. The instantaneous field of 18.3 m/s clearly reflects the lower level of coherent shedding that is seen at that speed in both the velocity and surface pressure spectra. A given instantaneous field for 0.5 m/s on the modified edge is more difficult to visually distinguish from that of 1.5 m/s. (No figure is presented.) However, a visual survey of a large sampling of images does suggest the lesser level of shedding coherence seen in the spectra.

The mean velocity profiles at x/C=1.002 for the speeds of 0.5, 1.5, and 18.3 m/s are plotted for comparison as Fig 16. The relationship between shedding strength and the mean suction side shear layer gradient is evident. In order of increasing shedding strength, the test conditions are 18.3, 0.5, and 1.5 m/s. The same order of speeds applies to increasing suction side shear layer gradient. However, the pressure side shear layer gradient is maximum for the 0.5 m/s case. This may suggest that the pressure side shear layer is playing a lesser role than the suction side in determining the shedding. The pressure side shear layers are more similar and for all test conditions are relatively steep compared to the suction side profiles. Since the pressure side shear layer is less stable, shedding may for these geometries be governed by the stability of the suction side layer. Alternately, the shedding strength may be correlated not to the magnitude of the suction side gradient, but rather to the symmetry between the pressure and suction side shear layers. The 1.5 m/s case is also the case of greatest symmetry. It is difficult to visually judge whether 0.5 or 18.3 m/s would take second place on grounds of symmetry. For the data presented, the role of symmetry is difficult to separate from the impact of the suction side shear layer gradient.

Fig. 4a plots the suction side boundary layer upstream of separation, and reveals the source of the variation with Re_C in the suction side portion of the initial shear layer profile: the same variation is apparent in the suction side boundary layers. Though the data is not available, it is reasonable to expect that the variation in the pressure side shear layers is

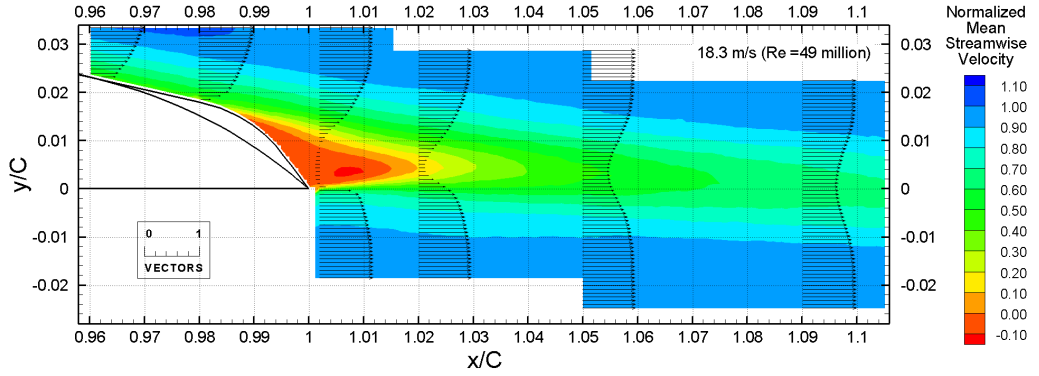


Figure 14. Average contours and vector profiles of normalized streamwise velocity, $\overline{u}/U_{ref}$, for the modified trailing edge at $U_{ref} = 18.3 m/s$. (320 Averages)

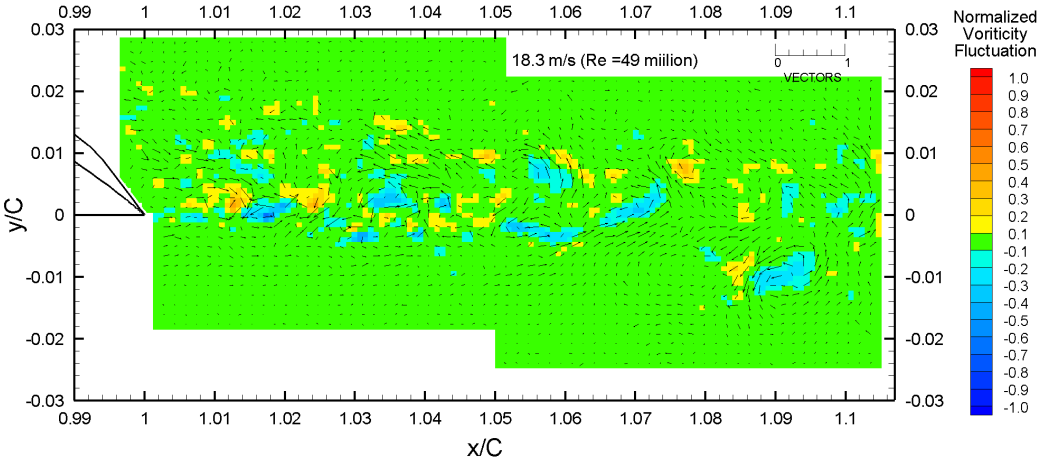


Figure 15. Instantaneous contour of normalized instantaneous vorticity fluctuation, $(\omega - \overline{\omega})\delta^* / U_{ref}$, and vector field of normalized instantaneous velocity fluctuations, $[(u-\overline{u}),(v-\overline{v})]/U_{ref}$, for the modified trailing edge at $U_{ref} = 18.3 m/s$.

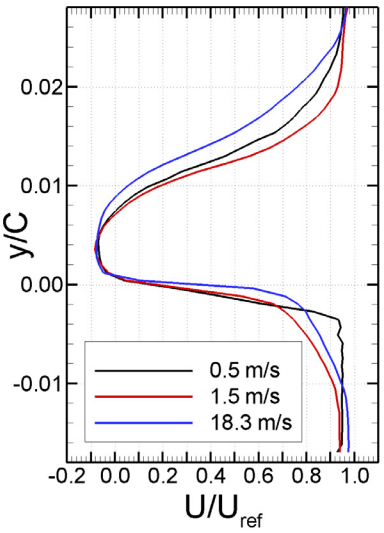


Figure 16. Comparison of normalized mean streamwise velocity profiles, $\overline{u}/U_{ref}$, for varying flow speed, U_{ref} , at x/C=1.002 on the modified trailing edge .

likewise found in the pressure side boundary layers. It has not been determined to what degree the shedding behavior is influencing the upstream boundary layers. However, the mean profile variation observed is consistent with the Re-dependent location of transition and boundary layer growth rates discussed earlier. Hence the Re-dependence of the shedding may be linked through the mean suction side boundary layer profile to the Re-dependence of transition and growth rate of the suction side boundary layer.

SUMMARY AND CONCLUSIONS

In summary, selected results have been presented from the second and third phases of the High Reynolds Number Hydrofoil Project, for which flow features of two trailing edge geometries were measured at Re_C from 0.25 to 61 million. Dependence of trailing edge vortex shedding on both trailing edge geometry and Re_C is demonstrated in the PIV vector fields, the LDV-acquired wake velocity spectra, and in the dynamic surface pressure spectra. For both geometry and Re_C variation, shedding strength was correlated with the predominant slope of the initial mean suction side shear layer, and possibly with the symmetry between the initial suction and pressure side shear layers. Beyond the potential importance of suction/pressure side symmetry, the pressure side shear layer did not appear to play as significant a role as the suction side in governing shedding behavior. Re-dependence of the shear layer gradients is a result of the Re-dependence of the naturally transitioning and developing boundary layers. 1.5 m/s emerged as both a maximum shedding case and the speed below which suction side transition becomes fixed at the adverse pressure gradient cliff in the C_p curve. Similar behavior would be expected of actual naval propulsors, though surface roughness would push the fixed-transition condition to lower speeds. These findings invite further study on the relationship of the mean shear layer profiles to shedding behavior behind turbulent hydrofoils. The influence of the location of transition on the shedding strength raises practical questions concerning tripping practices in model testing and the appropriate application of those results to the full scale.

ACKNOWLEDGEMENTS

The authors of this paper wish to the acknowledge the contributions of Shiyao Bian and Kent Pruss of the University of Michigan; William Blake, Ken Edens, Bob Etter, Ted Farabee, Jon Gershfeld, Joe Gorski, Tom Mathews, David Schwartzenberg, Jim Valentine, Phil Yarnall, Joel Park, and the LCC technical staff from the Naval Surface Warfare Center - Carderock Division; and Ki-han Kim, Pat Purtell and Candace Wark from the Office of Naval Research. In addition, the authors wish to thank the Office of Naval Research for supporting this research effort under contract nos. N00014-99-1-0341, and N00014-99-1-0856.

REFERENCES

Arabshahi, A., Beddhu, M., Briley, W., Chen, J., Gaither, A., Janus, J., Jaing, M., Marcum, D., McGinley, J., Pankajakshan, R., Remotigue, M., Sheng, C., Sreenivas, K., Taylor, L., and Whitfield, D., "A perspective on naval hydrodynamic flow simulation," 22nd Symposium on Naval Hydrodynamics ,National Academy Press, Washington, DC, 1999, pp. 920-934.

Blake, W.K. Mechanics of Flow Induced Sound and Vibration, Vol. 2, Academic Press, Orlando, 1986.

Bourgoyne, D. A., Ceccio, S. L., Dowling, D. R., Jessup, S., Park, J., Brewer, W., and Pankajakshan, R., "Hydrofoil Turbulent Boundary Layer Spearation at High Reynolds Numbers," 23nd Symposium on Naval Hydrodynamics, Val de Reuil, France, National Research Council, 2001A.

Bourgoyne, D. A., Judge, C. Q., Hamel, J. M., Ceccio, S. L., and Dowling, D. R., :Lifting Surface Flow, Pressure, and Vibration at High Reynolds Number," Proceedings of the 2001 International Mechanical Engineering Conference and Exposition, N.Y., NY, Amer. Soc. of Mech. Eng., 2001B.

Fourguette, D., Modarass, D., Taugwalder, F., Wilson, D., Koochesfahani, M., and Gharib, M., "Miniature and MOEMS Flow Sensors," AIAA paper no. 2001-2982, 2001.

Vetterling, W. T., Teukolsky, S. A., Press, W. H., and Flannery, B. P., Numerical Recipes in C, Second Edition, Cambridge University Press, Cambridge, U.K., 1992.

Wang, M., Lele, S.K., and Moin, P., "Computation of Quadrapole Noise Using Acoustic Analogy," AIAA Journal, Vol. 34., 1996, pp. 2247-2254.

White, F.M., Viscous Fluid Flow, 2nd Ed. McGraw Hill, Inc., New York, 1991, pp. 433-435.

APPENDIX A: ERROR ANALYSIS OF THE VELOCITY SPECTRA MEASUREMENTS

The spectral analysis of the velocity fluctuations in the hydrofoil wake was performed using data provided by the LDV and data reduction capabilities of the BSA Flow software provided by Dantec. The spectrum tool within the BSA software estimates the power spectral density from the raw data-samples using sample/hold re-sampling and FFT-techniques.

The BSA Flow software allows for three user inputs for the power spectra: spectral samples, maximum frequency, and filter settings. The spectral-samples input determines the number of discrete frequencies at which the power spectral density is estimated. As the spectral analysis is FFT-based, the software limits this user defined setting to an integer power of 2. The maximum frequency determines the highest frequency at which the power spectral density is estimated, and it was maintained at approximately 2 ~ 3 times the mean data rate for the data reported in this study to eliminate aliasing. Although not a user defined variable, the mean data rate acts as a third variable necessary to define the spectrum because the combination of the random seeding particle arrivals for the LDV and the sample-and-hold re-sampling technique acts as a first order low-pass filter. The cut-off frequency for this pseudo-filter occurs at $\dot{n}/2\pi$, where $\dot{n}$ is the mean data rate. Lastly, the data were filtered with a Hanning window with a filter width of W = 0.2. A summary of the spectral samples, maximum frequencies, and data rates for the data provided in Figures 9 and 10 is provided in Table 2.

The power spectral density, PSD, is defined by Equation (6) where $\Phi_v(f)$ is the PSD, T is the maximum lag time, V is the Fourier transform of the velocity time series, u(t), as defined by Equation (7), and V* is the complex conjugate of V.

$$\Phi_v(f) = \frac{1}{T} V^*(f,T) V(f,T) \tag{6}$$

$$V(f,T) = \int_0^T \left(v(t) - \bar{v}\right) e^{-i2\pi ft} dt \tag{7}$$

The physical relationship between the variance, shown in terms of the RMS value (within the flow and the power spectrum) is given by Equation 8.

$$v_{rms} = \left(2 \cdot \int_0^\infty \Phi_v(f) df \right)^{1/2} \tag{8}$$

The definition of the spectra above is based on the assumed knowledge of the true continuous signal v(t). However, in the actual LDV-based experiment, the time history records are not continuous. For an LDV-based experiment, a velocity sample occurs whenever a seeding particle passes through the measuring volume. Because of the randomness of this occurrence, the time history of the flow is provided by a discrete representation with sequential arrival times of varying incremental time steps. Without the knowledge of a continuous time history, only an estimate of the spectra is possible. The accuracy of the spectra decreases significantly above the mean data rate. Because the LDV measurements are non-continuous, The Dantec BSA Flow software employs the use of the sample/hold method as described by Equation (9). The sampled

	Baseline Trailing Edge				Modified Trailing Edge			
Velocity	Spectral Samples	Maximum Frequency	Data Rate	Cut-Off Frequency	Spectral Samples	Maximum Frequency	Data Rate	Cut-Off Frequency
U_{ref}	N		$\dot{n}$	$\dot{n}/2\pi$	N		$\dot{n}$	$\dot{n}/2\pi$
(m/s)		(s^{-1})	(s^{-1})	(s^{-1})		(s^{-1})	(s^{-1})	(s^{-1})
0.5	8192	500	251	40	8192	300	156	25
0.75	8192	700	342	54	8192	500	213	34
1.0	16384	1000	388	62	16384	800	343	55
1.5	16384	1500	593	94	16384	1500	531	85
3.0	32768	3000	1121	178	32768	3000	869	138
6.0	32768	7000	3138	499	32768	7000	2591	412
18.3	65536	10000	6366	1013	65536	10000	5190	826

Table 2. A summary of the spectral samples, maximum frequencies, and data rates for the LDV-acquired velocity spectra of Figs. 9 and 10.

and held signal is re-sampled at regular intervals to provide a series of evenly distributed velocity samples.

$$\left\{ v_{resamp}(t) = v(t_i) \middle| (t_i \le t \le t_{i+1}) \right\} \qquad (9)$$

Inaccuracies due to this simplistic approach occur when two neighboring true samples are further apart than the time between re-samples. For the spectra presented, the re-sampling rate, defined as twice the maximum frequency, is maintained at approximately 3 to 6 times the data rate. Assuming a Poisson distribution for the particle arrival within a homogeneous, random distribution of seeding particles in the fluid, the loss of information due to re-sampling is 1 ~ 4%. The loss information during the hold periods acts like a first-order low pass filter attenuating the spectrum at frequencies above f = $\dot{n}/2\pi$. For the data provided in Figures 9 and 10, the attenuation of the signal above the cut-off frequency should result in a slightly lower calculated RMS level as compared to the actual RMS. The re-sampled data results in a 0.6% reduction, for 1.0 m/s with the modified trailing edge, in the calculated v_{rms} using the spectrum as compared to the actual v_{rms} calculated using the raw time series data.

With the re-sampled data, the integral in the Fourier transform expressed in Equation (7) can be replaced with the summation given in Equation (10) where the term T/N = Δt is the re-sampling interval, N is the number of spectral samples, and each value of k represents a different frequency: f_k = k/T, k = 0, 1, 2, …, N/2.

$$V_k = \frac{T}{N}\sum_{n=0}^{N-1}(v_n - \bar{v})\exp\left(-i2\pi\frac{kn}{N}\right) \qquad (10)$$

This value is calculated using FFT-algorithms, and as before, the power spectrum estimate, shown in Equation (11), is derived by the multiplication of the V_k and its complex conjugate.

$$\Phi_k(f_k) = \frac{1}{T}V_k^* V_k \qquad (11)$$

APPENDIX B: THE RIGID HYDROFOIL APPROXIMATION

It is important to establish that the spectral peaks attributed in this paper to rigid hydrofoil fluid dynamics are not in fact due to resonances of a non-rigid structure. Such vibration would generate pressure spectral peaks (1) through inertial effects within the pressure sensor (independent of fluid pressures), (2) by generating surface pressure as the flow is forced by the surface motion, and (3) by more complex fluid-structure interactions. Figs. 17 and 18 compare the spectra of the pressure side pressure transducer 'H-1' at 99% of chord with that of a nearby accelerometer 'A2', at flow speeds of 18.3 and 1.5 m/s, respectively.

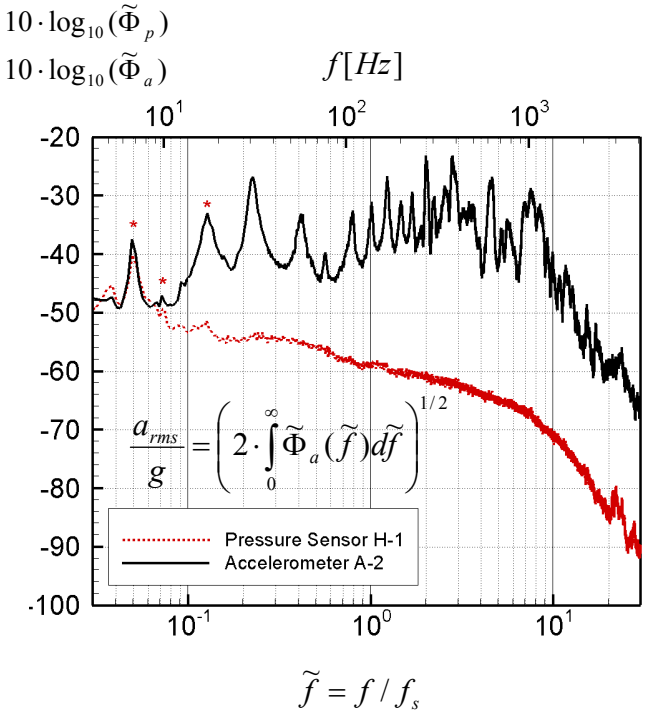


Figure 17. Comparison of normalized power spectra of surface pressure, $\tilde{\Phi}_p$, and normalized power spectra of foil acceleration, $\tilde{\Phi}_a$, for the pressure side sensor H-1 at x/C=0.99 and nearby accelerometer A2, at flow speed $U_{ref} = 18.3\,m/s$ on the modified trailing edge. At this flow speed f_s = 137 Hz.

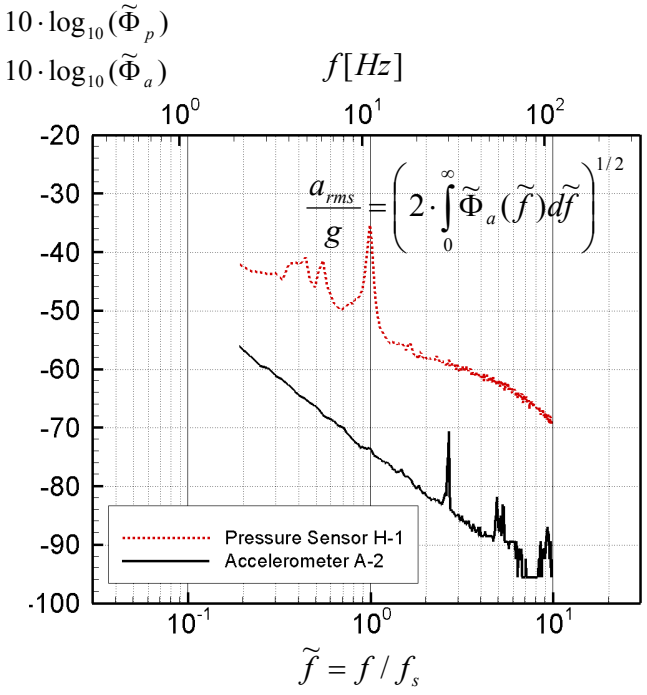


Figure 18. Comparison of normalized power spectra of surface pressure, $\widetilde{\Phi}_p$, and normalized power spectra of foil acceleration, $\widetilde{\Phi}_a$, for the pressure side sensor H-1 at x/C=0.99 and nearby accelerometer A2, at flow speed $U_{ref} = 1.5 m/s$ on the modified trailing edge. At this flow speed f_s = 11 Hz.

Normalization of the accelerometer spectra follows a form similar to that used with the velocity and pressure spectra:

$$\widetilde{\Phi}_a(\widetilde{f}) = \frac{\Phi_a \cdot f_s}{g^2} \qquad (12)$$

The relationship between the acceleration spectrum and the variance is given on the plot. These power spectra were produced in the same way as the pressure spectra presented earlier, except in this case no filtering was done. For convenience, the x-axis is given in both Hz and normalized frequency. The accelerometer selected is both the one nearest to the sensor and the one showing the highest accelerations. Both Figs. 17 and 18 confirm that the acceleration contamination effects are not present at significant levels in the frequency ranges of interest (near a normalized frequency of unity). Peaks in the accelerometer spectra at 18.3 m/s (Fig. 17) are reflected in the pressure spectra only at 7, 10, and 18 Hz (marked with asterisks). 18 Hz corresponds to the lowest natural frequency of the hydrofoil (beam bending between spanwise supports), and 7 Hz is both near both the channel impeller blade pass frequency and the channel flow-circuit lowest-mode acoustical frequency. Higher frequency peaks in the accelerometer spectra are not reflected in the pressure spectra, including the second natural frequency of the hydrofoil near 30 Hz. (The 30 Hz mode shape is a pitching motion about the spanwise mounts and would be particularly interactive with the vortex shedding.) Fig. 18 shows that at the maximum shedding case of 1.5 m/s, there is no correlation between the accelerometer and the pressure sensor, and there are no acceleration peaks near the shedding frequency. Maximum RMS acceleration levels at the four test speeds are provided in prior work (Bourgoyne, *et al*., 2001B) and the highest reported level is roughly 0.1g

A lack of fluid structure interaction is further supported by order-of-magnitude arguments comparing hydrofoil motion to the measured velocity fluctuations near the hydrofoil. Cyclic vertical hydrofoil motion or pitching about the spanwise supports would potentially generate an oscillation in the vertical flow velocities in the immediate vicinity of the leading and trailing edges. Conservatively assuming that the induced flows near the hydrofoil are of the same velocity as the hydrofoil surface, and assuming that the entire 0.1 g of acceleration is confined to the peak in Fig. 17 at 30 Hz, the trailing edge tip flow oscillations would be on the order of 0.1% of flow speed (U_{ref}=18.3 m/s). Vertical velocity fluctuations measured with LDV at the baseline trailing edge tip (Bourgoyne, et al., 2001A) are approximately 6% of the flow speed, so that the estimated flow generated by hydrofoil vibration would be roughly 1% of the actual measured vertical flow velocity fluctuation. These levels rapidly decrease with decreasing flow speed.